The submitted manuscript has been authored by a contractor of the U.S. Government under Contract No. DE-AC05-00OR22725. Accordingly, the U.S. Government retains a nonexclusive royalty-free license to publish or reproduce the published form of this contribution, or allow others to do so, for U.S. Government purposes.

A self-organized critical transport model based on critical-gradient fluctuation dynamics*

L. Garcia

Universidad Carlos III, 28911 Leganés, Madrid, Spain

B. A. Carreras

Oak Ridge National Laboratory, Oak Ridge, Tennessee 37831-8070, U.S.A.

D. E. Newman

Department of Physics, University of Alaska, Fairbanks, Alaska, U. S. A.

ABSTRACT

A one-dimensional transport model based on critical-gradient fluctuation dynamics is presented. This model has the characteristic properties of a self–organized critical (SOC) system. As the source increases and for an input flux above a threshold value, a dynamical transition spontaneously takes place. A high-gradient edge region forms. The width of this region increases with increasing value of the particle source. Transport dynamics in this edge region self-organizes to be very close to marginal stability, while the core remains at the subcritical gradient that is typical of an SOC system.

PACs: 52.55.Hc, 52.65.Kj, 52.35.Ra

---

* Research sponsored by the Office of Fusion Energy, U.S. Department of Energy, under contract DE-AC05-00OR22725 with UT-Battelle, LLC, and Cooperative Agreement DE-FC02-99ER54512.

I. INTRODUCTION

In the past 10 years, there has been great interest in the concept of self-organized criticality (SOC)[1] as a unifying explanation for some of the observed universal dynamics of complex systems. Characteristic SOC dynamics can explain some of the properties of transport in magnetically confined plasmas[2,3] and transitions to high-confinement regimes.[4-6] It also offers a new perspective on how plasma transport and fluctuation dynamics calculations should be performed.[7,8]

Here we consider a one–dimensional transport model based on critical-gradient fluctuation dynamics. The fluctuation dynamics is incorporated through an evolution equation for the fluctuation envelope as has been done in models like Ref. 9. This equation is coupled to a transport equation for a scalar quantity h. For convenience, we will refer to this quantity as particle density. Transport is controlled by the fluctuation level, and the fluctuations are triggered when the gradient of h is above a critical value. We can interpret[3] each radial site as corresponding to a resonant surface, and the coupling to the transport is done through the amount of flux transported in each resonant surface. This model includes both fluctuation and transport timescales. It has the characteristic properties of an SOC system such as subcritical transport, probability distribution function (PDF) with power tails, and expected power spectra. However, in contrast with the sandpile model, transport is not done by an integer amount of grains of sand, but by a continuous amount that is regulated by the local fluctuations.

As the particle source increases, a dynamical transition spontaneously takes place. For a particle flux above a threshold value, an edge pedestal like region forms, and the pedestal width increases with increasing value of the particle source. Transport in this edge region self-organizes to be very close to marginal stability, while the core remains at the subcritical gradient that is typical of the sandpile. The two regions are characterized by distinct dynamical behavior of the fluxes. The change from one radial region to the other is sharp and has the characteristic properties of a transition.

The control parameter for the transition is the local mean flux. When the mean particle flux is low, the transport is caused by bursty flux events. The system remains subcritical most of the time and evolves through a sequence of particles bursts. At the

critical value of the local mean flux, this mechanism cannot effectively keep the particle balance, and the system transitions to another state. In this state, the gradient of the particle density stays very close to its critical value, z_c, and the flux becomes continuous with intermittent changes of its amplitude.

The rest of this paper is organized as follows. In Sec. II, we present the transport model, and we discuss its numerical implementation. In Sec. III, a description of the numerical results is given. This is followed, in Sec. IV, by an analysis of the dynamics of the fluxes that allows us to characterize the transition. Finally, In Sec. V, we discuss the results and conclusions of this paper.

II. EQUATIONS OF THE MODEL AND NUMERICAL SCHEME

The model proposed in this paper consists of two equations describing the evolution of the root-mean-square (rms) fluctuations, $\Phi(x)$, and of the averaged density, $h(x)$. The two equations are

$$\frac{\partial \Phi}{\partial t} = \Phi(\gamma - \mu\Phi) + S_1, \tag{1}$$

$$\frac{\partial h}{\partial t} = \frac{\partial}{\partial x}\left(\mu_0 \Phi \frac{\partial h}{\partial x}\right) + S_0. \tag{2}$$

In the fluctuation equation, γ is the linear growth rate of the instability, μ is the coefficient of the nonlinear term that is responsible for the saturation of the turbulence, and the third term, S_1, is a small source term to guarantee a minimal level of seed fluctuations. This seed for fluctuations is needed to start the growth when the profile goes from supercritical to subcritical. The transport equation includes two terms: a source term, S_0 and a radial diffusion term. In the latter, we assume that the diffusivity is proportional to the level of fluctuations and is given by $\mu_0\Phi$.

The underlying instability is assumed to be a critical-gradient instability. Then the linear growth rate is

$$\gamma = \gamma_0 \left(-\frac{\partial h}{\partial x} - z_c\right) \Theta\left(-\frac{\partial h}{\partial x} - z_c\right). \tag{3}$$

Here, Θ is the Heaviside function, and z_c is the absolute value of the critical gradient. The source terms are not continuous, but they represent the random addition of fluctuation energy and density with a prescribed probability. In Eq. (1), we add $\overline{\Phi}$ with probability p_1, in Eq. (2), we add an amount δ with probability p_0.

This model represents a generalization of the classical sandpile model used to interpret plasma transport[3] by the addition of fluctuation dynamics that regulates the amount of transport, which couples back to the fluctuations through the gradient drive.

Equations (1) and (2) can be rewritten in dimensionless form as

$$\frac{\partial \hat{\Phi}}{\partial \tau} = \hat{\Phi}\left(\hat{\gamma} - \hat{\Phi}\right) + \hat{S}_1 , \tag{4}$$

$$\frac{\partial \hat{h}}{\partial \tau} = \frac{\partial}{\partial \hat{x}} \left(\hat{\Phi} \frac{\partial \hat{h}}{\partial \hat{x}}\right) + \hat{S}_0 . \tag{5}$$

Here, $\tau = t\gamma_0 Z_c$, $\hat{x} = x\sqrt{\mu/\mu_0}$, $\hat{h} = \left(h/Z_c\right)\sqrt{\mu/\mu_0}$, $\hat{\Phi} = \mu\Phi/\left(\gamma_0 Z_c\right)$, $\hat{\gamma} = \gamma/\left(\gamma_0 Z_c\right)$, $\hat{S}_1 = \mu S_1/\left(\gamma_0 Z_c\right)^2$, and $\hat{S}_0 = \left(S_0/Z_c^2\right)\sqrt{\mu/\left(\mu_0 \gamma_0^2\right)}$. There are no explicit parametric dependencies in these equations except for the source term. However, they depend on the system size $\hat{L} = L\sqrt{\mu/\mu_0}$. Because of this transformation, in what follows we take $\gamma_0 = 1$.

Equations (1) and (2) are numerically advanced in the following way. First, the source terms are taken into account by

$$\Phi_i^t \rightarrow \Phi_i^t + \overline{\Phi} \tag{6}$$

with probability p_1, and

$$h_i^t \rightarrow h_i^t + \delta \tag{7}$$

with probability p_0. Then we proceed to time advance by setting

$$\Phi_i^{t+\Delta t} = \Phi_i^t \exp\left[\Delta t\left(\gamma_i - \mu\Phi_i^t\right)\right] , \tag{8}$$

$$h_i^{t+\Delta t} = h_i^t + \Delta t\mu_0\left(-\Phi_i^{t+\Delta t} z_i + \Phi_{i-1}^{t+\Delta t} z_{i-1}\right) , \tag{9}$$

for $i > 0$. At the origin

$$h_0^{t+\Delta t} = h_0^t - \Delta t\mu_0 \Phi_0^{t+\Delta t} z_0 , \tag{10}$$

where $\gamma = (z - z_c)\Theta(z - z_c)$, with $z_i = h_i^t - h_{i+1}^t$.

The boundary condition at the edge, $x = L$, is $h_{\text{edge}} \equiv h(L) = 0$. Note that Φ_i is really defined at i+1/2, and $\Phi(L)$ does not enter in the scheme.

The form for the time advancement of Φ, Eq. (8), has been chosen to guarantee the positivity of the fluctuation amplitude.

III. NUMERICAL RESULTS

Using the model described in the previous section, we have carried out numerical calculations for different values of the parameters. For these calculations, a time step of $\Delta t = 0.05$ has been used. The time evolution goes through a transient phase. The length of this phase depends on the size L of the system. After the transient, there is a steady state phase. The function h in steady state can be characterized by its slope z. The time-averaged fluctuation profile must be such that the induced local flux at every location is equal to the input flux, that is $\mu_0\langle\Phi_i z_i\rangle = p_0 x_i$.

Because the diffusion coefficient is proportional to Φ and the source term in Eq. (1) is random with a fixed size step, this source term (if large enough) can induce diffusive transport. In the radial region where the randomly induced flux is larger than the fluctuation-induced flux, $p_1\overline{\Phi} > \Delta t\langle\gamma_i \Phi_i\rangle$, diffusion dominates, and the slope of z is

linear with x. In this region, the time-averaged Φ is given by $\langle \Phi_i \rangle = \sqrt{p_1 \overline{\Phi} / (\mu \Delta t)}$ and is essentially independent of the radial position [Fig. 1(a)]. When $p_1 \overline{\Phi} < \Delta t \langle \gamma_i \Phi_i \rangle$, the fluctuation-induced flux dominates; the saturation condition for the fluctuations is $\langle \gamma_i \rangle = \mu \langle \Phi_i \rangle$; and because the slope of z is nearly constant, the $\langle \Phi \rangle$ profile is approximately linear with x [Fig. 1(a)]. In this diffusion-dominated regime, one can reproduce many of the properties identified in the case of combining a sandpile dynamics with diffusive transport.[10] Therefore, depending on the value of p_1 and $\overline{\Phi}$, we can have a diffusion dominated transport [Fig. 1(a)], or an avalanche-dominated transport regime [Fig. 1(b)]. In the remainder of this paper, we always work in the second regime where the effect of the source term S_1 on the transport dynamics is negligible.

As expected,[11] and from the invariance transformation given in the previous section, numerical results are not affected by the value of the critical gradient, z_c. Therefore, we keep $z_c = 5$ for all cases considered here. This independence of z_c is a consequence of the simple form of this model. Here, we consider a single instability mechanism. In more realistic models, multiple instabilities are possible, each with its own critical gradient. In such a case, a dependence on the relative magnitude of the critical gradients may appear. We also keep constant throughout these calculations the amount of density added randomly to the h, that is $\delta = 0.05$, and we control the particle source through the frequency p_0 of these additions. The probability p_1 is maintained very small. The only role of this term is to avoid the fluctuations going to zero during the subcritical phase. We keep the value of p_1 below 10^{-7}, and for this range of values the numerical results are independent of p_1. Therefore, we are left with three main parameters: p_0, L, and μ_0/μ. To understand the role of each parameter, we have done sequences of numerical calculations that vary each of these parameters independently. For the p_0–scans, we set $\mu_0/\mu = 0.5$ and considered four values of L—100, 200, 400, and 800.

As a difference from the classical sandpile, the system is not always subcritical. The average slope can be below z_c but can also be at marginal stability, $z = z_c$. How much of the profile is subcritical depends on the value of p_0. An example is shown in Fig. 2,

where we have plotted the time-averaged slope of h for different values of p_0. The results plotted in Fig. 2 are for a system's length L = 200.

In Fig. 2, we see the jump in the averaged slope of the density at a given radial position. This jump is sharp and has the characteristic properties of a transition. It is not only a change in the averaged equilibrium properties of the sandpile, but also reflects a change in transport dynamics as discussed in the next section. The transition point from subcritical to marginal is well defined in all cases. It is also clearly visible in the averaged profile of the fluctuations (Fig. 1). This transition point depends on both p_0 and the system size, L. For each one of the four sequences of p_0-scan calculations with different size L, we can plot the position of transition point as a function of p_0. In this way, we obtain four self-similar curves. As can be seen in Fig. 3, these four curves can be superimposed by plotting them as a function of the parameter $p_0L^{3/4}$. The functional dependence on this parameter is simple and can be described by the following:

$$\frac{x_m}{L-20} = \frac{1}{\left(p_0 L^{3/4}/A\right)^{5/2}+1} . \tag{11}$$

Here, the value of the parameter A = 0.0067 has been determined by fitting this function to the data. In this figure, we have normalized x_m to L–20 instead of L. The reason is that boundary effects can be important in a range of about 10 cells in each of the end points of the radial region.

By transforming Eqs. (1) and (2) to Eqs. (4) and (5), we have shown that, apart from z_c, only two relevant parameters remain: the renormalized source $\hat{S}_0 = S_0\sqrt{\mu/\left(\mu_0\gamma_0^2\right)}$ and the system size $\hat{L} = L\sqrt{\mu/\mu_0}$. For the time-averaged h profile, the renormalization of the source can be interpreted as a renormalization of p_0. Therefore, Eq. (11) automatically can be changed to include the dependence in the parameter μ/μ_0 in the following way:

$$\frac{x_m}{L-20} = \frac{1}{\left[p_0 L^{3/4}(\mu/2\mu_0)^{7/8}/A\right]^{5/2}+1} . \tag{12}$$

In Fig. 4, we compare the fit obtained from the numerical data for $\mu_0/\mu = 0.5$ with the data for $\mu_0/\mu \neq 0.5$. As expected, the agreement is good.

For very low values of the averaged flux, p_0L, the jump in the slope stays just at the edge. This is the case for $p_0 = 10^{-6}$, shown in Fig. 2, and for lower values of p_0. From Eq. (12), we have that the pedestal width is greater than one cell for

$$p_0 L \geq A \left(\frac{2\mu_0}{\mu} \right)^{7/8} L^{-3/2} . \tag{13}$$

For values of p_0L above this value, the jump on the slope moves inward, and the edge pedestal broadens. We can interpret Eq. (13) as a threshold value for the total particle flux.

IV. ANALYSIS OF THE NUMERICAL RESULTS

The slope of the density gradient as a function of the radial position x near the jump region has the properties of a critical transition. The real control parameter for the transition is not necessarily x, but it is probably the time-averaged local flux $\Gamma = p_0x$. One of the properties that allows us to identify the change in slope as a transition is that the width of the transition region decreases in relation to the system size with increasing system size.

We calculate the width W_S of the transition region by fitting the slope with a constant plus a hyperbolic tangent. In Fig. 5, we show an example of such a fit and the parameters W_S and x_m are indicated in the figure. When x_m is close to any of the boundaries, the width becomes very small. However, for values of x_m such as $0.2L \leq x_m \leq 0.8L$, W_S is approximately constant for a fixed system size. When L increases, W_S increases as $L^{0.4}$. This scaling is shown in Fig. 6, where we have plotted

$W_S / L^{0.4}$ as a function of x_m/L for all cases considered. We can see that, within error bars, all points fall on top of the same curve.

To understand the transition between subcritical and marginal regions of the profile, it is important to investigate the dynamical properties of the fluxes in the different radial positions or averaged local flux values. To do so, time sequences of the fluxes for radial points around the transition point have been analyzed. The time sequences of fluxes are 2×10^8 points in length.

The mean value of the flux does not have any particular radial structure in the region of the transition point. This, of course, is expected because the mean flux has to match the integrated source, which is uniform in x. However, there is a different dynamical behavior of the fluxes above and below the transition point. A way to visualize this change in behavior is to do a two-dimensional (2-D) plot of the contours of the flux. Such a plot is shown in Fig. 7. Between the transition point (x = 161) and the edge, there is continuous activity. In the inner region, the activity is sporadic. In this region, the dominant transport mechanism is avalanche transport. These avalanches are triggered in the outer region (x > 161), and they propagate inward (x < 161). They can penetrate all the way to the center of the pile (x = 0). Some avalanches may start in the inner region (x < 161), but they are rare, and it takes a long time for them to build up. Although most avalanches propagate inward, all fluxes are positive, which causes outward transport of particles. If we look at the time trace of the fluxes, the flux is bursty for $x < x_m$. It is practically zero most of the time, and suddenly a flux burst occurs. Above the transition radius, there is a continuous flux with what looks like a superimposed noise.

To quantify the change of behavior of the fluxes, it is useful to introduce the parameter Λ. This parameter is defined as the ratio of the time-averaged, most probable flux (the maximum of the PDF of the fluxes) to the time-averaged flux. In Fig. 8, we have plotted Λ as a function of x/x_m for 20 different cases, which vary from p_0 and L. In the radial region where the flux is bursty, we see that $0 < \Lambda < 0.3$. That is, the large values of the flux that dominate the tail of the PDF determine the mean flux. In this

region, Λ is bound to a low value, but its value varies from case to case without a clear pattern. At the transition point, Λ jumps above 0.8 for all cases considered and goes asymptotically to 1 for $x/x_m > 1$. In this region, $x/x_m > 1$, the mean flux is determined by the peak of the PDF. Although the function $\Lambda(x/x_m)$ is not a universal function, the functional form is quite close for all cases considered.

The change of Λ with x is very sharp at $x/x_m = 1$, and again it shows the characteristics of a transition. From case to case and in the region $x/x_m = 1$, there is a slight change on the rate of increase of Λ with x. We can measure this rate of increase and, from it, calculate the width W_Γ of the transition region. In Fig. 9, we have plotted W_Γ/x_m for all the cases considered as a function of p_0. This figure shows that the W_Γ/x_m on p_0 is compatible with a simple power scaling.

This transition from a continuous flux to intermittent flux is rather similar to the transition discussed in Ref. [12] for a pure sandpile model. However, in the latter case the transition was observed as an overall change of the dynamics of the sandpile, while in the present model the change appears at a radial position.

Other statistical properties of the flux depend on the radial position or mean flux, and they correlate with the transition points. An example can be seen in Fig. 10, where we have plotted the variance of the flux for each of the sequences with $L = 800$ and different values of p_0 as a function of x/x_m. There is a clear sharp peak of the variance at the transition point.

This change in the value of the variance reflects a qualitative change of the PDF of the fluxes, $P(\Gamma)$, as we move from the subcritical to the marginal region. For $L = 800$ and $p_0 = 5 \times 10^{-5}$, we have illustrated this change by plotting the normalized PDF for the different radial positions (Fig. 11). In this figure, we have plotted the PDF at each radial point multiplied by x of the flux normalized to x, $xP(\Gamma/x)$. In this way, the mean is the same for all the PDFs. In the subcritical region the tails of the large positive fluxes are all on top of each other, and they scale as a power, $xP(\Gamma/x) \rightarrow \lambda(\Gamma/x)^{\alpha}$. Clearly, above the transition point, there is a change in the functional form of the PDF, and the large flux tail

no longer lies on top of the others. For the region of normalized fluxes between 10^{-6} and 10^{-5}, we can calculate the decay index α of this tail. The results for the same sequence are plotted in Fig. 12. A similar plot can be done for a constant p_0 scan varying L. This is shown in Fig. 13. As can be seen from both figures, the exponent of the tail for large and positive fluxes is fairly constant and $2.0 < \alpha < 2.2$; but it increases sharply at the transition point. This value of α in the subcritical region indicates that the mean flux may be well defined, but its variance is unbounded.

We can verify better this PDF characterization by looking separately at some of these PDFs. First, consider the PDF of fluxes well in the subcritical region (Fig. 14). This PDF is strongly asymmetric with a clear algebraic tail. This algebraic tail is well defined over more than a decade of values of the flux. However, in the marginal region, the PDF is completely different. The bulk is well described by a Gaussian curve, but it is somewhat asymmetric (Fig. 15) with a weak tail. Therefore, the flux fluctuation can be approximately described by a mean value with Gaussian noise. Naturally, in this case the flux has a small level of intermittency. In this regime, the range of large positive fluxes that constitutes the algebraic tail is rather short and ill defined. Consequently, it is more difficult to determine the decay index of the PDF in this region (see Figs. 12 and 13).

One possible explanation for the transition follows: as the drive increases, the flux through all local positions must increase. This must be accommodated by the increased local effective diffusivity, because the system is in steady state, and we know that while the gradient changes it does not change by a large amount. Therefore from $\Gamma = D \quad h$, the effective diffusivity must increase to match the increased flux. Note that with a distributed source, this is true for simply changing radial position as well as increasing the drive because the steady state flux through a given point is the integral of the drive inside that point. The low-flux state is characterized by the bursty intermittent transport events. The burst of particles comes into a radial location from the uphill side. If the site becomes unstable, the fluctuations grow until the fluctuation-induced flux reduces the gradient enough so that it is subcritical. At that time the fluctuations damp out (do not stop instantaneously) and leave the site at least somewhat subcritical. The high-flux state is characterized by more continuous lower level fluctuations. The "material" comes in

from uphill, which makes the site unstable. The fluctuations grow and transport the particles until it is subcritical; but before the fluctuations can turn off fully, the flux from above refills the local gradient, which starts the process again. The transition between states then occurs when the refill rate exceeds the flux from an individual burst. At that point, the average gradient will increase close to the critical gradient, and the fluctuations will change from bursty to more continuous with smaller oscillations. In this way, in the high-flux regime, the PDF of the fluctuations grows narrower and more Gaussian. This change is a consequence of the oscillations around the continuous level being driven by the random variations in the external drive. They are not caused by the collective effects of reaching and then relaxing away from the critical gradient that characterizes the low-flux transport regime.

V. DISCUSSION AND CONCLUSIONS

The one-dimensional transport model presented in this paper has the properties of an SOC system. The main transport mechanism is avalanche-like transport that leads to outward particle fluxes of all sizes. The distribution of fluxes has a power scaling tail with a decay index close to -2. In the inner region, the time-averaged slope of the particle density is significantly below the critical slope in spite of the local flux mechanism being a continuous variable controlled by the fluctuations instead of an integer quantity as in the case of the running sandpile. This model seeks to bridge the gap between the simple cellular automata models and the more complete "primitive" turbulence models. In the primitive turbulence models, exploring different regimes is difficult due to computational limitations; in the cellular automata models, much interesting physics is excluded due to the simplicity and discrete nature of the models.

This critical-gradient fluctuation-driven transport model shows the characteristic properties of a critical transition with control parameter the averaged particle flux, $\langle \Gamma \rangle = p_0 x$. When the mean particle flux is low, the transport is caused by bursty flux events. The system remains subcritical most of the time and evolves through a sequence of particle bursts. As the mean particle flux increases, the bursts have to happen more

often and be larger. At the critical value of $\langle\Gamma\rangle$, this mechanism cannot effectively keep the particle balance, and the system transitions to another state. In this state, the gradient of the particle density stays very close to its critical value, z_c, and the flux becomes continuous with intermittent changes of its amplitude.

This model shows that even in a very simple system spontaneous transitions can occur. Such a transition in this system will cause an effective confinement improvement simply by establishing a region with an increased gradient. Furthermore, this model predicts a detectable global flux threshold for this transition. This threshold depends on the parameter regulating the saturation of the fluctuations and the particle transport coefficient in the "lower-confinement" regime. It is important to note that the nature of the transition is not likely to be directly related to the “classical” enhanced confinement regimes since the physics thought to be responsible for those regimes is not included in this model. Rather, it defines a region, for example an edge region, in which the dynamics are different and the gradient is increased making this the region in which a “classical” confinement enhancement transition can occur. This is because the requisite features for a transition to enhanced confinement, namely inhomogeneity of the turbulence and a broken symmetry in the fluctuations, both exist. The former comes from the transition point itself while the latter comes from the increased gradient. This type of “transition” makes the most sense near the edge. However, depending on the parameters and instabilities involved, this transition could also occur in the core.

ACKNOWLEDGMENTS

The authors gratefully acknowledge very stimulating and useful discussions with Diego del-Castillo-Negrete. This research is sponsored by the Dirección General de Investigación (Spain) under Project No. FTN2000-0924-C03-01. Part of this research has been performed at Oak Ridge National Laboratory, managed by UT-Battelle, LLC, for the U.S. Department of Energy under contract number DE-AC05-00OR22725 and at Univ. of Alaska under contract number DE-FG03-99ER54551.

REFERENCES

[1]P. Bak, C. Tang, and K. Weisenfeld, Phys. Rev. Lett. **59,** 381-4 (1987).

[2]P. H. Diamond, and T. S. Hahm, Phys. Plasmas **2,** 3640 (1995).

[3]D. E. Newman, B. A. Carreras, P. H. Diamond, and T. S. Hahm, Phys. Plasmas **3,** 1858-66 (1996).

[4]D. E. Newman, B. A. Carreras, and P. H. Diamond, Phys. Lett. A **218**, 58 (1996b).

[5]S. C. Chapman, R. O. Dendy, and B. Hnat, Phys. Rev. Lett. **86**, 2814 (2001).

[6]H. R. Hicks and B. A. Carreras, Phys. Plasmas **8** (2001).

[7]B. A. Carreras, D. Newman, V. E. Lynch, and P. H. Diamond, Phys. Plasmas **3,** 2903-2911 (1996).

[8]X. Garbet and R. E. Waltz, Phys. Plasmas **5,** 2836 (1998).

[9] P. H. Diamond, V. B. Lebedev, D. E. Newman, and B. A. Carreras, Phys. Plasmas, **2**, 3685 (1995).

[10] R. Sanchez, D. E. Newman, B. A. Carreras, Nucl. Fusion **41**, 247 (2001).

[11]L. P. Kadanoff, S. R. Nagel, L. Wu, and S. M. Zhou, *Phys. Rev. A* **39**, 6524 (1989)

[12]A. Corral and M. Paczuski, Phys. Rev. Letters **83**, 572 (1999).

FIGURE CAPTIONS

FIG. 1. Time-averaged fluctuation level and slope of h for : (a) $p_0 = 1 \times 10^{-4}$, $p_1 = 1 \times 10^{-3}$, and $\bar{\varphi} = 1 \times 10^{-5}$ (diffusion-dominated regime) and (b) $p_0 = 1 \times 10^{-4}$, $p_1 = 1 \times 10^{-7}$, $\bar{\varphi} = 1 \times 10^{-8}$ (avalanche dominated regime).

FIG. 2. Time-averaged slope of h for different values of p_0. The figure shows the change of the jump position in the averaged slope.

FIG. 3. Radial position of the transition normalized to the system size as a function of the parameter $p_0 L^{3/4}$ for different sizes of the system and $\mu_0/\mu = 0.5$.

FIG. 4. A generalization of the plot in Fig. 3 by transformation of variables. In this plot, we compare the fit obtained from the numerical data for $\mu_0/\mu = 0.5$ with the data for $\mu_0/\mu \neq 0.5$.

FIG. 5. Width, W_S, and position, x_m, of the transition as determined from a fit to the numerically calculated averaged slope for a case with $p_0 = 10^{-4}$.

FIG. 6. Finite-size scaling of the width of the transition region as a function of x_m/L.

FIG. 7. A 2-D plot of the contours of the flux in the time-radius plane to show the time evolution of the radial structure of the flux.

FIG. 8. Ratio of the time-averaged, most probable flux [the maximum of the PDF of the fluxes] to the time-averaged flux as a function of x/x_m for 20 different cases varying p_0 and L.

FIG. 9. Normalized radial width of the transition region of Λ as a function of p_0.

FIG. 10. Variance of the flux for each of the sequences with L = 800 and different values of p_0 as a function of x/x_m.

FIG. 11. PDF of the flux normalized to x, $xP(\Gamma/x)$ at several values of the radial position x.

FIG. 12. Decay index α of the algebraic tail of the PDF of normalized fluxes in the range 10^{-6} to 10^{-5}, for different values of p_0.

FIG. 13. Decay index α of the algebraic tail of the PDF of normalized fluxes in the range 10^{-6} to 10^{-5}, for different values of L.

FIG. 14. An example of a PDF of fluxes well in the subcritical region.

FIG. 15. An example of a PDF of fluxes well in the marginal region.

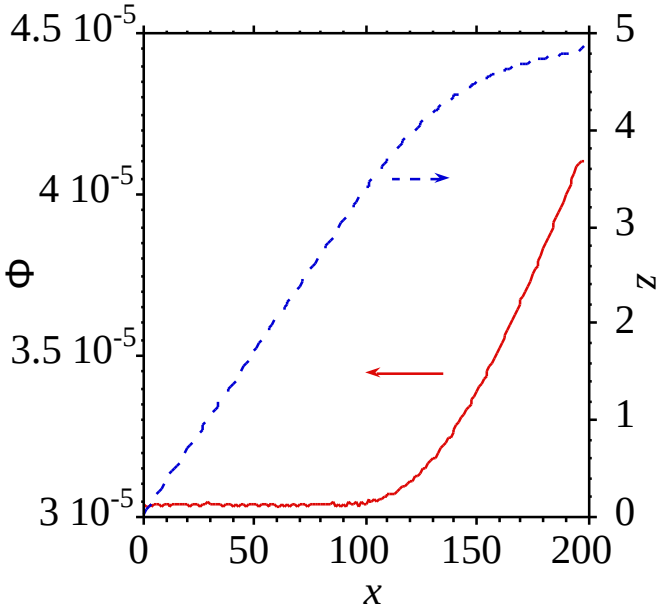
4.5 10-5
4 10-5
3.5 10-5
3 10-5
Φ
5
4
3
2
1
0
z
0
50
100
150
200
x

Fig. 1(a)

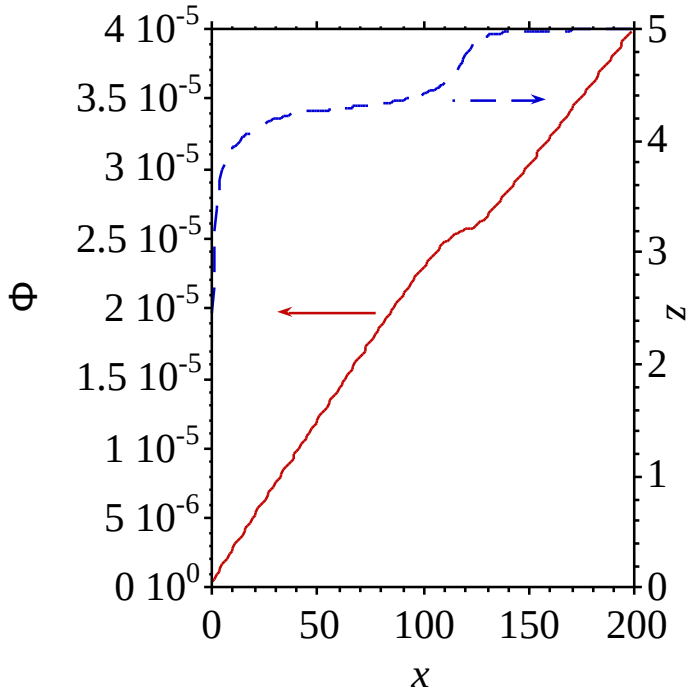
4 10-5
3.5 10-5
3 10-5
2.5 10-5
2 10-5
1.5 10-5
1 10-5
5 10-6
0 100
Φ
5
4
3
2
1
0
z
0
50
100
150
200
x

Fig. 1(b)

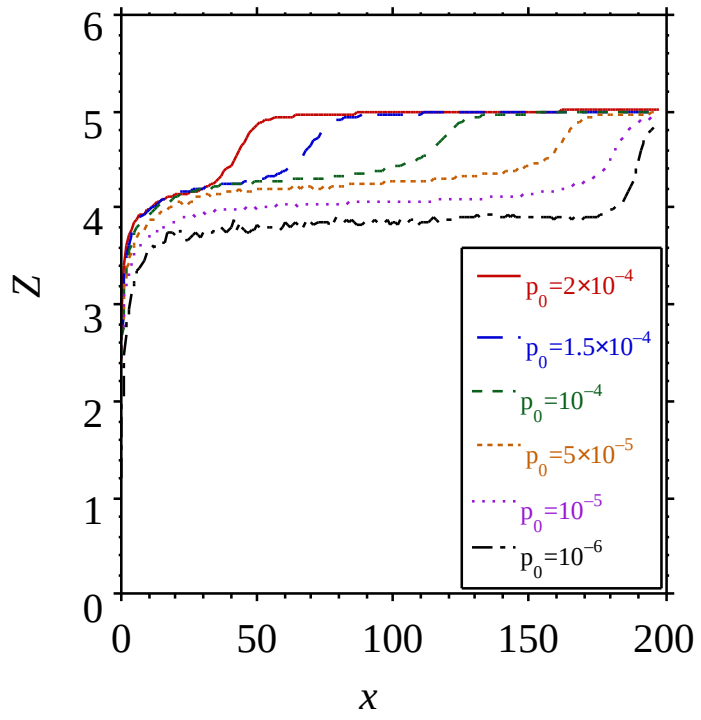
6
5
4
3
2
1
0
Z
0
50
100
150
200
x
p0=2×10−4
p0=1.5×10−4
p0=10−4
p0=5×10−5
p0=10−5
p0=10−6

Fig. 2

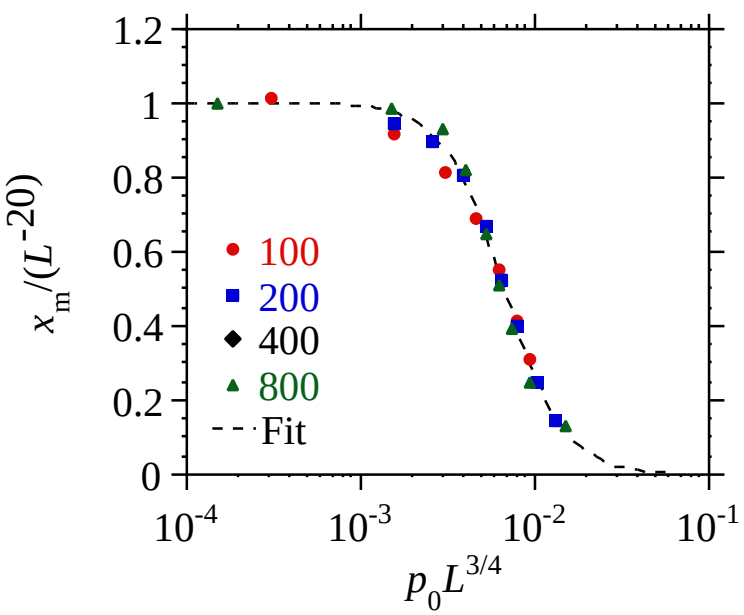
1.2
1
0.8
0.6
0.4
0.2
0
xm/(L-20)
100
200
400
800
Fit
10-4
10-3
10-2
10-1
p0L3/4

Fig. 3

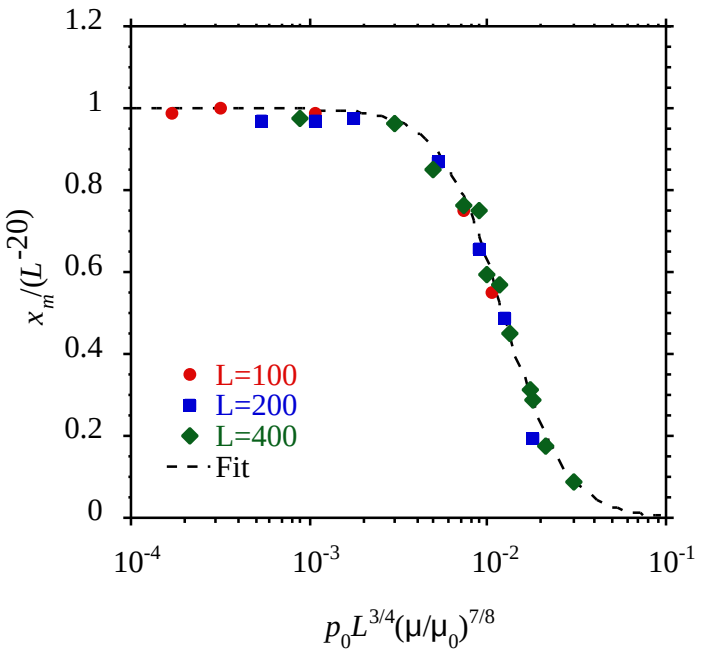
1.2
1
0.8
0.6
0.4
0.2
0
$x_m/(L^{-20})$
L=100
L=200
L=400
Fit
10^{-4}
10^{-3}
10^{-2}
10^{-1}
$p_0L^{3/4}(\mu/\mu_0)^{7/8}$

Fig. 4

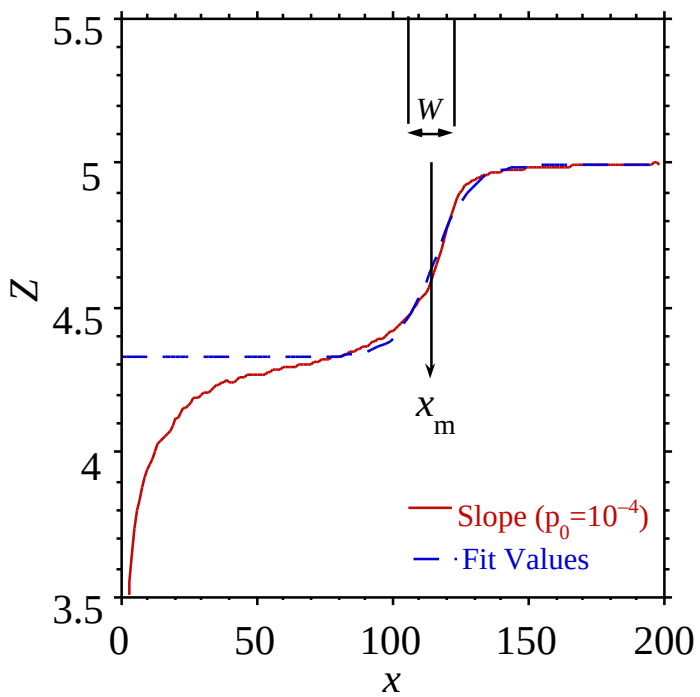
5.5
5
4.5
4
3.5
Z
W
x_m
Slope ($p_0=10^{-4}$)
Fit Values
0
50
100
150
200
x

Fig. 5

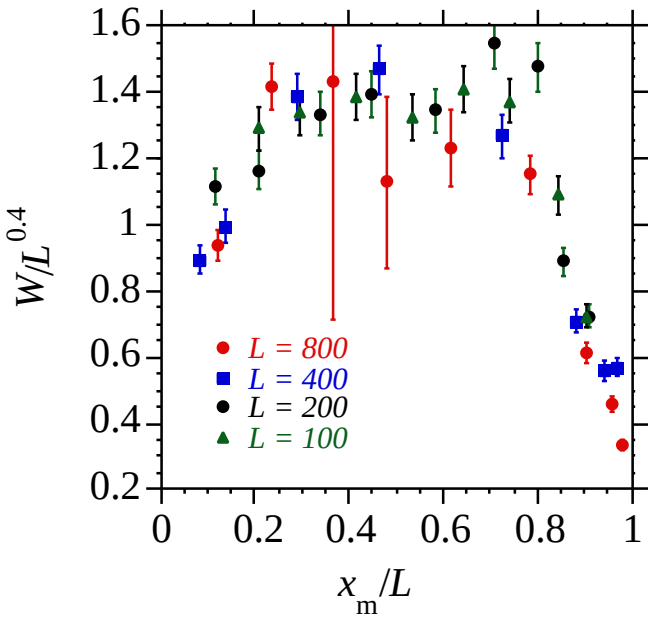

Fig. 6

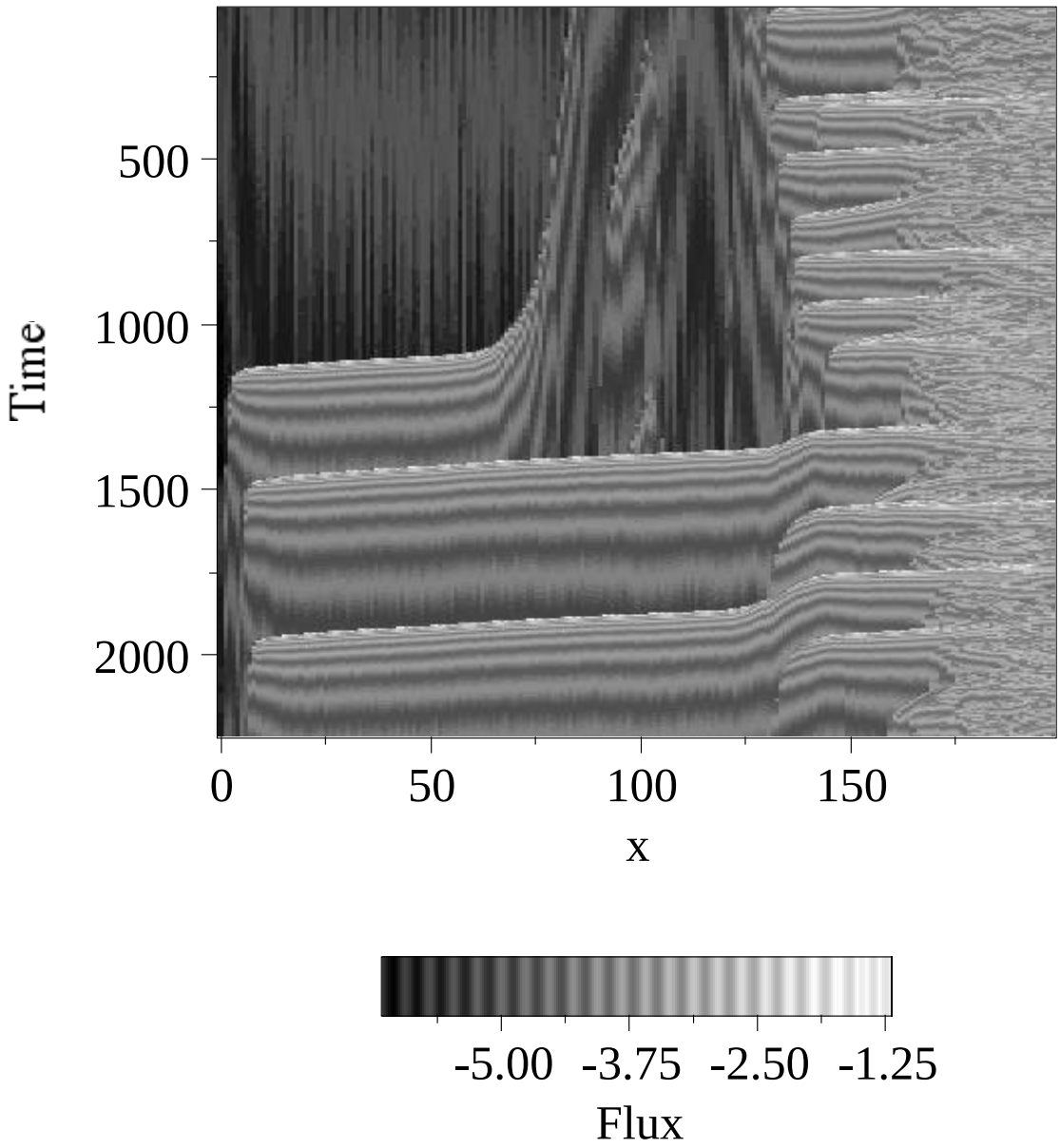

Fig. 7

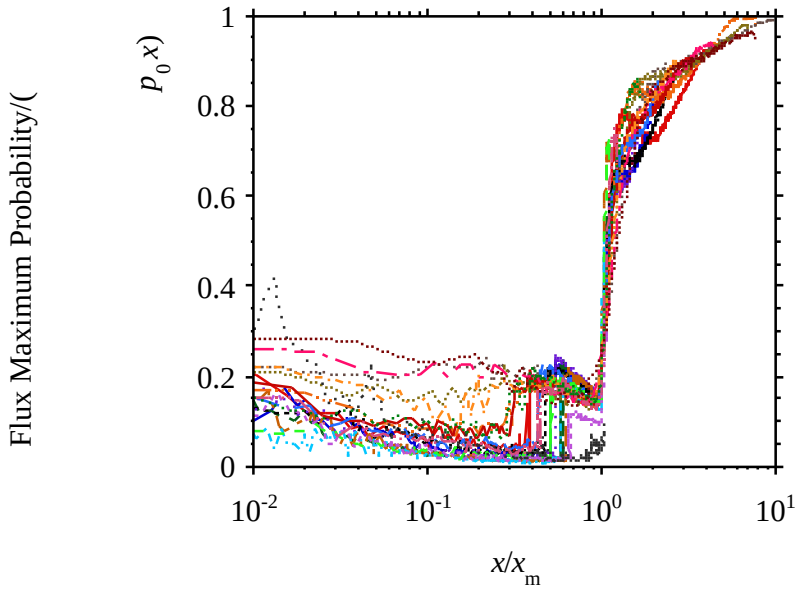
Flux Maximum Probability/(
$p_0 x$)
1
0.8
0.6
0.4
0.2
0
10^{-2}
10^{-1}
10^{0}
10^{1}
x/x_m

Fig. 8

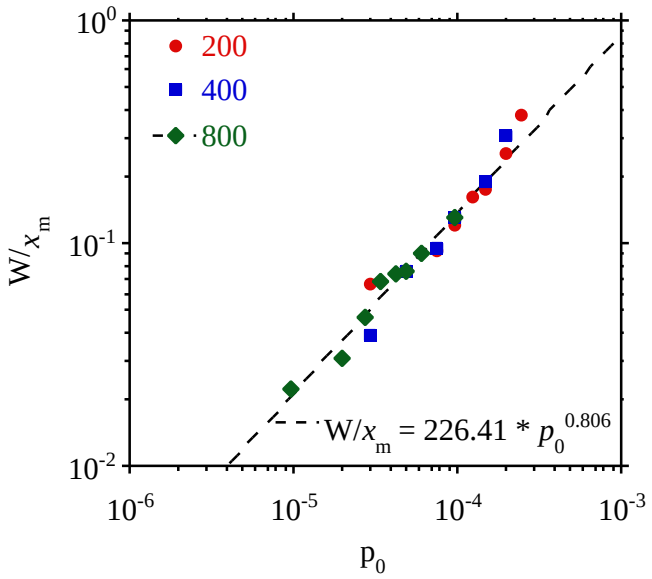
10^{0}
10^{-1}
10^{-2}
W/x_m
200
400
800
$W/x_m = 226.41 * p_0^{0.806}$
10^{-6}
10^{-5}
10^{-4}
10^{-3}
p_0

Fig. 9

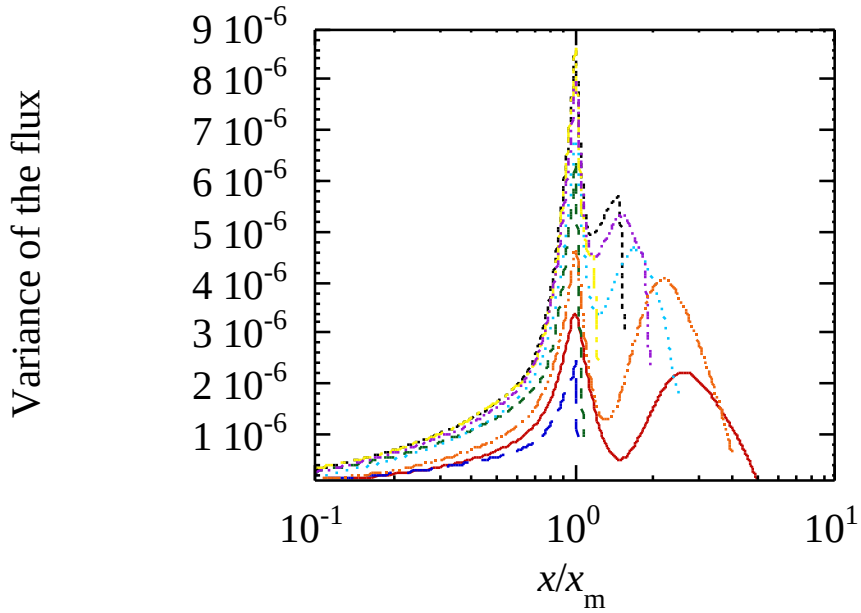
Variance of the flux
9 10-6
8 10-6
7 10-6
6 10-6
5 10-6
4 10-6
3 10-6
2 10-6
1 10-6
10-1
100
101
x/xm

Fig. 10

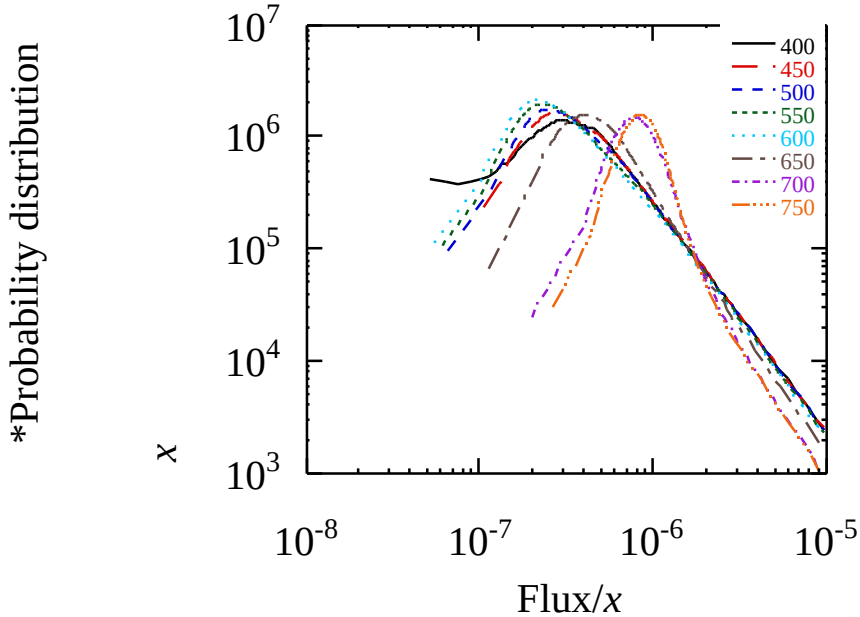
*Probability distribution
x
107
106
105
104
103
10-8
10-7
10-6
10-5
Flux/x
400
450
500
550
600
650
700
750

Fig. 11

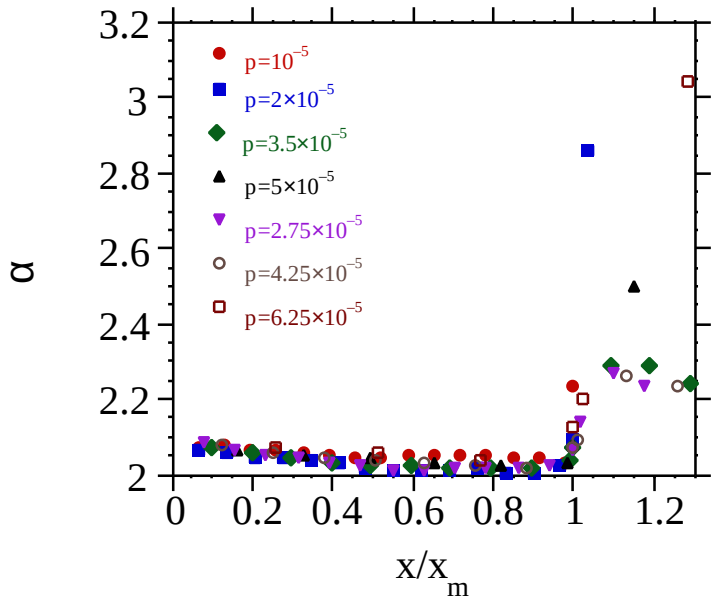
3.2
3
2.8
2.6
2.4
2.2
2
α
0
0.2
0.4
0.6
0.8
1
1.2
x/x_m
p=10^-5
p=2×10^-5
p=3.5×10^-5
p=5×10^-5
p=2.75×10^-5
p=4.25×10^-5
p=6.25×10^-5

Fig. 12

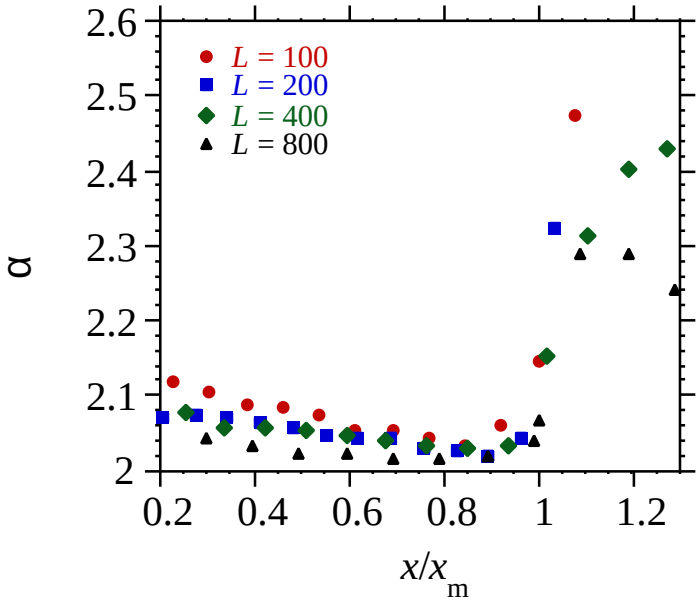
2.6
2.5
2.4
2.3
2.2
2.1
2
α
0.2
0.4
0.6
0.8
1
1.2
x/x_m
L = 100
L = 200
L = 400
L = 800

Fig. 13

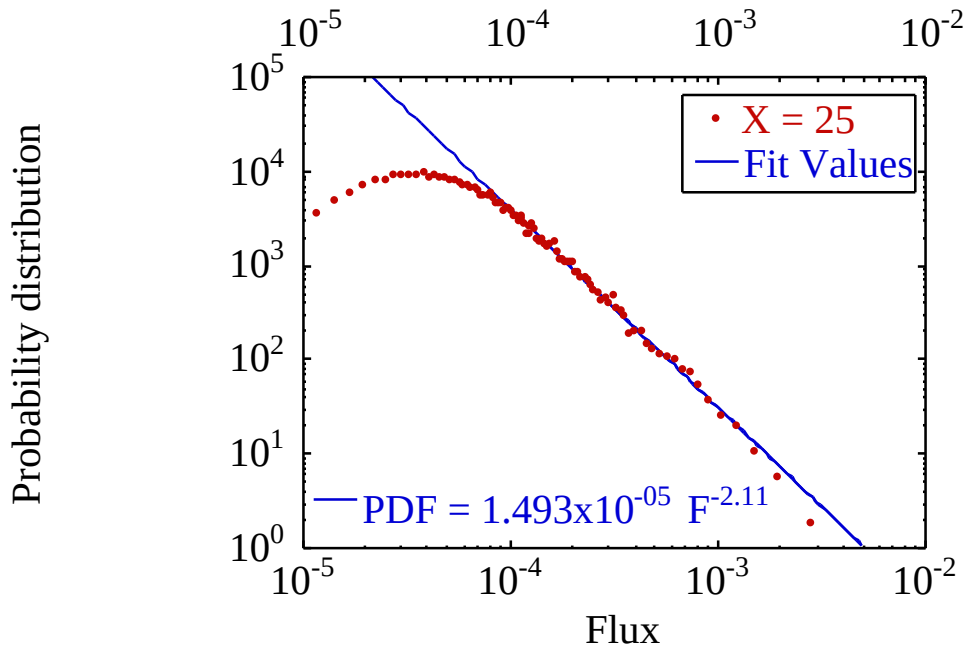
Probability distribution
Flux
X = 25
Fit Values
PDF = 1.493x10^-05 F^-2.11

Fig. 14

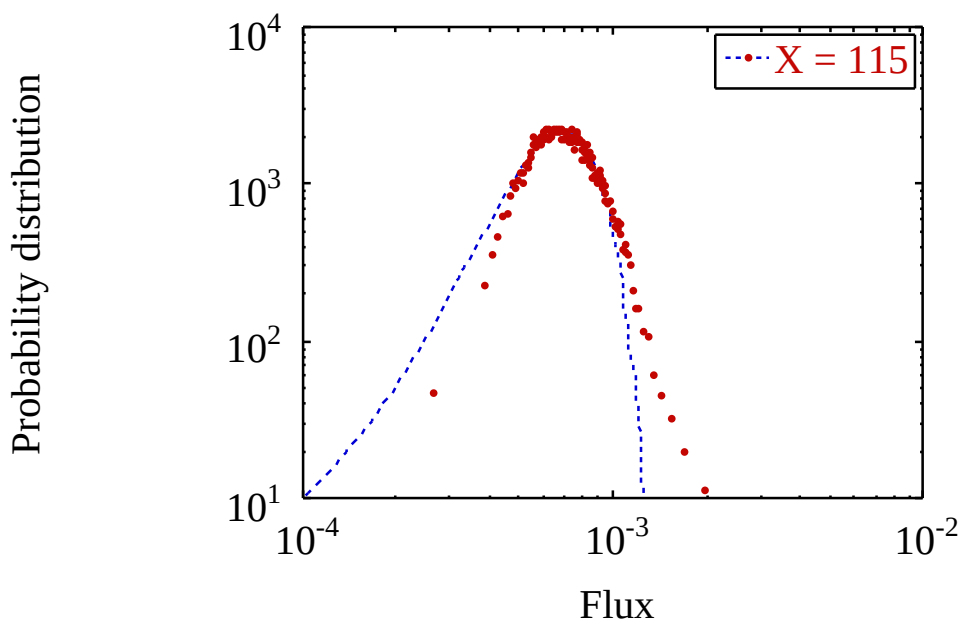
Probability distribution
Flux
X = 115

Fig. 15